



Aerothermodynamics of blunt body entry vehicles

Brian R. Hollis^{a,*}, Salvatore Borrelli^b

^a NASA Langley Research Center, Hampton, VA 23666, USA

^b CIRA Italian Aerospace Research Centre, Via Maiorise, 81083 Capua (CE), Italy

ARTICLE INFO

Available online 11 January 2012

Keywords:

Blunt body entry vehicles
Turbulent flow on blunt bodies
Rarefied flow
Radiation transport

ABSTRACT

In this chapter, the aerothermodynamic phenomena of blunt body entry vehicles are discussed. Four topics will be considered that present challenges to current computational modeling techniques for blunt body environments: turbulent flow, non-equilibrium flow, rarefied flow, and radiation transport. Examples of comparisons between computational tools to ground and flight-test data will be presented in order to illustrate the challenges existing in the numerical modeling of each of these phenomena and to provide test cases for evaluation of computational fluid dynamics (CFD) code predictions.

Published by Elsevier Ltd.

Contents

1. Blunt body entry vehicles overview	42
1.1. MSL background.	43
1.2. CEV background.	43
1.3. FIRE-II background.	44
2. Turbulent blunt-body flow	45
2.1. Mars Science Laboratory turbulent flow	45
2.2. Orion Crew Exploration Vehicle turbulent flow	45
2.2.1. CUBRC LENS testing of Orion CEV	45
2.2.2. AEDC tunnel 9 testing of Orion CEV	46
2.2.3. LaRC 20-Inch Mach 6 air testing of Orion CEV	47
3. Non-equilibrium blunt-body flow	47
3.1. Mars Science Laboratory non-equilibrium flow	48
3.1.1. CUBRC LENS testing of MSL	48
3.1.2. Caltech T5 testing of MSL	50
3.2. Orion Crew Exploration Vehicle non-equilibrium flow	51
4. Rarefied flow	52
5. Radiation transport	53
5.1. FIRE-II radiation transport	54
6. Summary, conclusions, and recommendations	54
Acknowledgments	55
References	55

1. Blunt body entry vehicles overview

Blunt body configurations are the most common geometries employed for entry into planetary atmospheres. Examples of manned blunt-body entry vehicles include the Mercury, Gemini, and Apollo capsules. Examples of unmanned flight test or

interplanetary probe blunt-body entry vehicles are more numerous and include the Viking, Pioneer, FIRE II, ARD, OREX, Stardust, etc. An overview of major programs that includes vehicle and mission descriptions in which blunt body entry vehicles have been employed is given in [1].

In broad terms, a blunt-body entry vehicle is comprised of a large heat shield that protects a smaller crew cabin or robotic probe payload. The heat shield is generally axisymmetric, with either a large-angle, sphere-cone geometry (e.g. the Mars Viking probe) or a large radius-of-curvature spherical cap (e.g. the Apollo

* Corresponding author.

E-mail address: brian.r.hollis@nasa.gov (B.R. Hollis).

command module), although asymmetric shapes have sometimes been considered (e.g. the canceled Aeroassist Flight Experiment).

The geometry of the heat shield produces large amounts of aerodynamic drag that decelerate the vehicle from orbital or interplanetary speeds. A small amount of aerodynamic lift for maneuverability and cross-range capability may also be provided by offsetting the center-of-gravity of the vehicle to trim it at a non-zero angle of attack.

The heat shield material, which is either a high-temperature insulator or an ablative material, protects the payload from the high levels of convective heating, and in some cases, radiative heating experienced during atmospheric entry. The large effective radius of the blunt body heat shield acts to mitigate the effects of convective heat transfer. However, the large radius actually has the opposite effect with respect to radiative heating, but radiation is typically a smaller fraction of the maximum heat rate and an even smaller fraction of the total integrated heat load.

The effects of non-equilibrium chemical and vibrational processes and of radiation transport have long been recognized as challenging applications of Computational Fluid Dynamics (CFD) tools used in the simulation of blunt body flow-fields. More recently, it has been recognized that some vehicles now in the developmental stage, e.g. the Mars Science Laboratory and Orion Crew Exploration Vehicle, will also experience environments that will be dominated by turbulent flow owing to their large sizes, high reentry velocities, and non-zero angle of attack lifting trajectories. The modeling of turbulent flow fields in the subsonic or low Mach number flow behind the bow shock of such vehicles presents a new challenge for CFD since experimental data on such flows are sparse. Research into radiative transport phenomena

has also generally languished since the 1970s (after work on the Jupiter Galileo program) without any actual missions in which aerothermodynamic radiation was a significant factor. More recently, missions such as Stardust, Huygens, and Orion have renewed the need for research and development of better computational models for radiative transport processes.

In this discussion of blunt-body aerothermodynamic phenomena, ground and flight test programs and supporting computational analyses will be discussed for several programs: the Mars Science Laboratory, the Orion Crew Exploration Vehicle, and the Fire II flight test. Brief overviews of each vehicle and mission are presented below.

1.1. MSL background

The Mars Science Laboratory (MSL) mission [2], to be launched in 2011, will deliver the largest (> 900 kg) rover ever to Mars (Fig. 1). The MSL will fly a controlled, lifting trajectory ($\alpha = 16^\circ$) to deliver the payload to within 10 km of the target location. The entry vehicle (Fig. 2) is comprised of a 4.5 m diameter spherically-blunted, 70-deg half-angle cone forebody heat shield that protects the aftbody payload from entry heating and provides a lift-to-drag (L/D) ratio of 0.24 for aerodynamic control and maneuvering. The MSL vehicle will enter the Martian atmosphere at a velocity of 5.6 km/s, which is greater than that of any other Mars probe except Mars Pathfinder. Because of the vehicle's large heat shield diameter and the high angle of attack and velocity of its entry trajectory, it is expected that the vehicle will experience boundary-layer transition to turbulent flow well before the peak heating point on its trajectory. Therefore the vehicle's Thermal Protection System (TPS) was designed [3,4] with a conservative assumption of turbulent flow throughout the entire trajectory. Extensive aerothermodynamic ground-testing was conducted in support of MSL development, including testing in the AEDC Hypervelocity Tunnel 9, CUBRC LENS I, CUBRC LENS X, Caltech T5, and the NASA Langley Research Center (LaRC) 20-Inch Mach 6 Air Tunnel and is discussed in [5–12].

1.2. CEV background

The Project Orion Crew Exploration Vehicle (CEV) was defined by NASA's Exploration Systems Architecture Study [13] as NASA's next manned space vehicle. The CEV will support NASA's exploration missions by providing crew access to the International Space Station, the moon, and Mars. The geometry of the CEV (Fig. 3) is similar to that of Apollo – a spherical segment heat shield that



Fig. 1. Size comparison of Mars rovers—from left: Mars Science Laboratory (2011), Mars Exploration Rover (2003), Mars Pathfinder (1996).

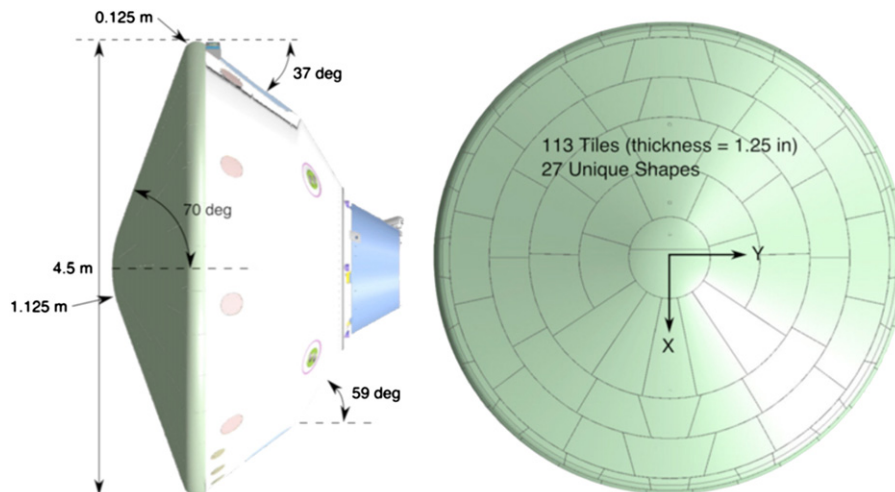


Fig. 2. Mars Science Laboratory entry vehicle.

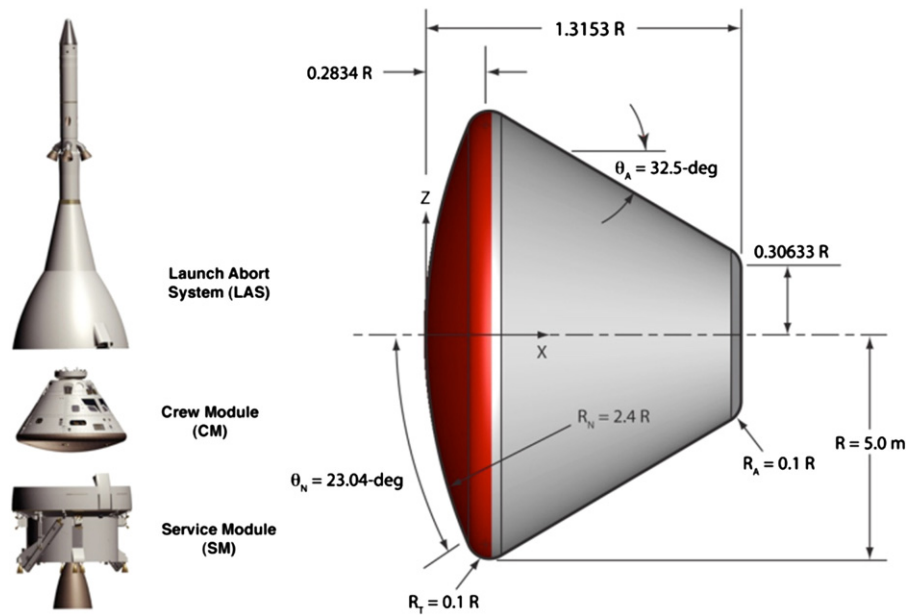


Fig. 3. Orion CEV crew module dimensions.

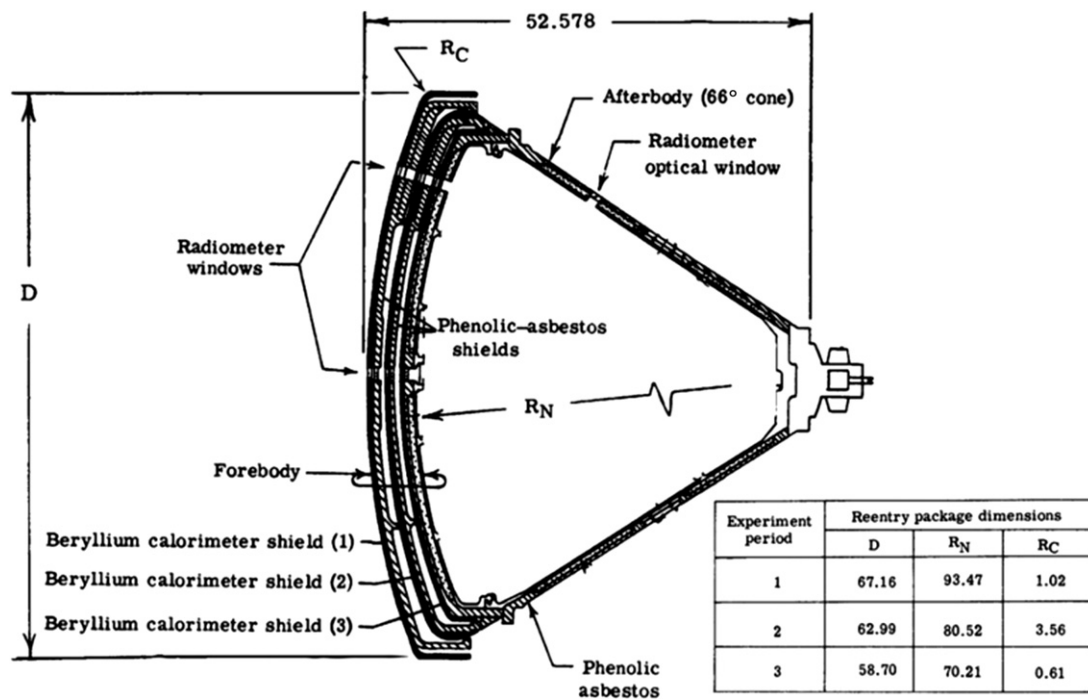


Fig. 4. Project FIRE vehicle dimensions.

protects a truncated-cone shaped crew compartment – but is considerably larger. The maximum diameter (current design iteration) of the CEV is 5 m, as compared to that of 3.912 m for Apollo.

The design of the CEV TPS must account for the high heating rates generated at lunar return velocities and the aerothermodynamic challenges of non-equilibrium thermo-chemistry, turbulent flow, and radiation transport. As with MSL, the CEV is being designed with the conservative assumption of fully-turbulent flow throughout its trajectory. Although not discussed herein, the CEV TPS design must also account for ablation effects, including shape change, flow field radiation-ablation coupling, and ablated surface roughness heating augmentation. Ground testing conducted in support of CEV development is discussed

in [14–22] and a summary of the overall test program is presented in [23].

1.3. FIRE-II background

Project FIRE (Flight Investigation of the Reentry Environment) was conducted expressly for the purpose of measuring radiative heating at Lunar return velocities. The FIRE-II mission, which flew in 1965, is generally considered to be the best documented data set available on radiative heating since the mission was explicitly designed for the measurement of radiative heat-transfer in a non-ablating environment. The FIRE-II vehicle (Fig. 4) was equipped with 3 separate beryllium heat shields that were each jettisoned

before they reached temperatures at which ablation would begin. Data were obtained with both integrated and spectrally-resolved radiometers and with total heat flux calorimeters on each heat shield. Mission details for FIRE-II are presented in [24,25] and flight test data are presented in detail in [26–28].

2. Turbulent blunt-body flow

Historically, turbulent flow at hypersonic speeds has generally been considered to be a design issue for moderate to high lift-to-drag ratio lifting bodies and winged vehicles, such as the Shuttle Orbiter. Such vehicles travel at high Reynolds numbers and their large size provides sufficient length over which turbulent flow can develop. In contrast, blunt-body reentry vehicles generally are smaller and have high drag coefficients that cause rapid deceleration, which thus decreases the likelihood of producing turbulent flow (Fig. 5).

However, the problem of turbulent heating has become important in recent blunt-body vehicle designs, notably the Mars Science Laboratory (MSL) and the Orion Crew Exploration Vehicle (CEV). Both these vehicles are, in comparison to past blunt-body vehicles, quite large: the MSL is 4.5 m diameter and the CEV will be ~ 5 m diameter. Furthermore, both vehicles will experience atmospheric entry (at Mars and Earth, respectively) at high speeds (~ 11 km/s for CEV and ~ 5 km/s for MSL) and fly high angle-of-attack (for blunt bodies) lifting trajectories (11-deg to 16-deg range for MSL and 16-deg to 24-deg range for CEV). These factors all tend to promote transition to turbulent flow and thus the conservative design philosophy applied in both projects is to assume turbulent flow throughout their trajectories.

This assumption of turbulent flow led to the requirement to conduct high-Reynolds number hypersonic aeroheating testing on each vehicle in order to obtain turbulent heat transfer data for use in the evaluation of the CFD models employed in the design of each vehicle. Several examples of these experimental studies will be presented in which comparisons with CFD results have been performed.

2.1. Mars Science Laboratory turbulent flow

An investigation of turbulent aeroheating on the MSL vehicle [12] was conducted in the Arnold Engineering Development Center (AEDC) Hypervelocity Wind Tunnel No. 9 [29]. In this

study, aeroheating data were collected on a 6-in. (0.1524 m) diameter, coaxial thermocouple instrumented MSL model in perfect-gas N_2 flow at the tunnels Mach 8 and Mach 10 test conditions. Data were obtained at free stream Reynolds numbers of $4 \times 10^6/\text{ft}$ to $49 \times 10^6/\text{ft}$ at Mach 8 and at $1 \times 10^6/\text{ft}$ to $19 \times 10^6/\text{ft}$ at Mach 10 with angles-of-attack between 0-deg and 24-deg. Turbulent flow was produced over the leeside of the heat shield at the highest Mach 10 Reynolds number, while turbulent flow was produced over the entire heat shield (both leeside and windside) at the highest Mach 8 Reynolds number. The experimental uncertainty of the data was estimated to be $\pm 12\%$.

Laminar and turbulent perfect-gas comparisons to these data were performed using the LAURA code [30] with the algebraic Cebeci–Smith turbulent model being used for the turbulent cases. Comparisons between centerline data and predictions are shown for selected $\alpha = 16$ -deg cases in Fig. 6. Free stream conditions for these cases are listed in Table 1. For the Mach 10 cases, the laminar predictions and data were in close agreement at $Re_\infty = 4 \times 10^6/\text{ft}$ case, while at $Re_\infty = 19 \times 10^6/\text{ft}$, the laminar predictions matched the data on the windside of the forebody and the turbulent predictions matched the data on the leeside. For both Mach 8 cases, the turbulent predictions matched the data. Although the agreement between predictions and data was generally good for these cases, there were discrepancies around the stagnation point ($x/R \sim 0.4$) for all cases where measured heating rates were higher than either laminar or turbulent predictions

2.2. Orion Crew Exploration Vehicle turbulent flow

2.2.1. CUBRC LENS testing of Orion CEV

Turbulent aeroheating testing of the Orion CEV vehicle was conducted [19] in the Calspan University of Buffalo Research Center (CUBRC) Large Energy National Shock Tunnel (LENS) I Hypervelocity Reflected Shock Tunnel [31]. The wind tunnel model was 14-in. (0.3556 m) in diameter and was instrumented with both coaxial thermocouples and thin-film gages. Runs were performed at Mach 8 with a 20-deg angle of attack for Reynolds numbers between $0.8 \times 10^6/\text{ft}$ and $32 \times 10^6/\text{ft}$. Turbulent flow was produced on the leeside of the heat shield for Reynolds numbers of $9 \times 10^6/\text{ft}$ and higher and turbulent flow was produced over the entire heat shield for Reynolds numbers of $23 \times 10^6/\text{ft}$ and higher.

Predictions were performed using the DPLR [32] code for laminar flow and turbulent flow with Menter's SST model used for the turbulent cases at the conditions given in Table 2.

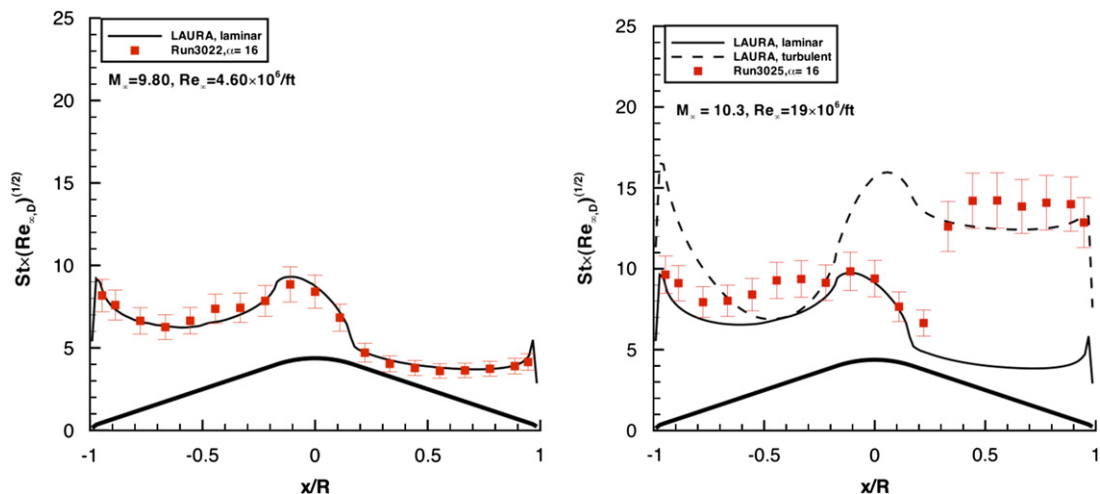


Fig. 5. MSL Mach 10, $\alpha = 16$ -deg data and comparisons from AEDC Tunnel 9.

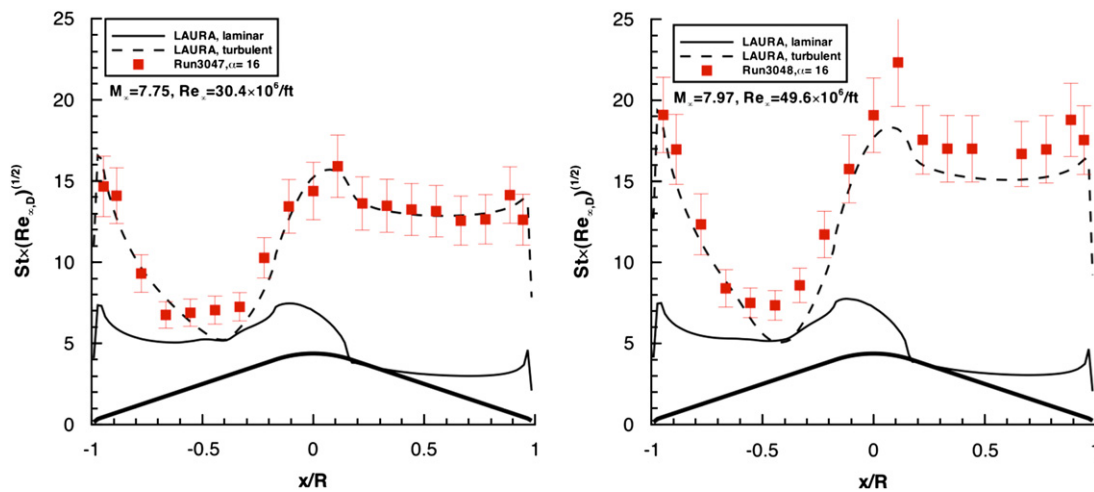


Fig. 6. MSL Mach 8, $\alpha=16$ -deg data and comparisons from AEDC Tunnel 9.

Table 1

MSL test conditions for AEDC Tunnel 9.

Run	α (deg.)	Re_{∞} (1/ft)	M_{∞}	P_{∞} (Pa)	T_{∞} (K)	ρ_{∞} (kg/m ³)	U_{∞} (m/s)
3022	16	4.62E+06	9.80	656.1	54.4	0.0406	1474.9
3025	16	1.91E+07	10.32	2068.1	48.3	0.1444	1461.8
3047	16	3.04E+07	7.75	8231.8	73.8	0.3760	1356.4
3048	16	4.96E+07	7.98	11918.6	69.3	0.5792	1350.9

Table 2

CEV test conditions for CUBRC LENS-I.

Run	α (deg.)	Re_{∞} (1/ft)	M_{∞}	P_{∞} (Pa)	T_{∞} (K)	ρ_{∞} (kg/m ³)	U_{∞} (m/s)
5	20	8.65E+05	7.64	260.8	79.8	0.0134	1371
11	20	3.10E+07	8.12	7791	74.4	0.366	1405
15	20	3.25E+07	7.96	8756	76.1	0.398	1396
21	20	29.7E+07	8.21	7033	71.7	0.339	1396

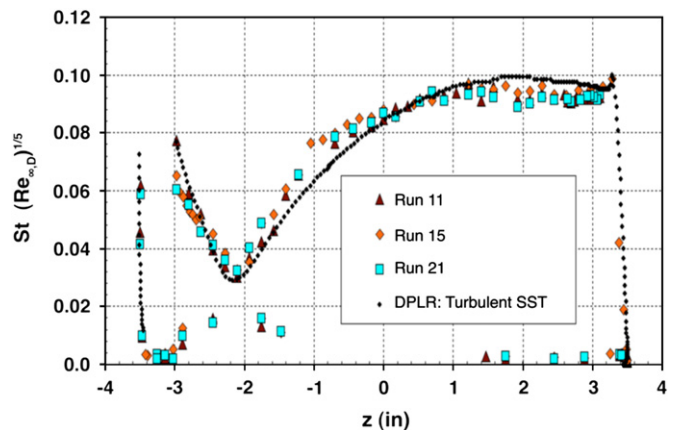


Fig. 8. CEV Mach 8, $\alpha=20$ -deg turbulent data and comparisons from CUBRC LENS-I.

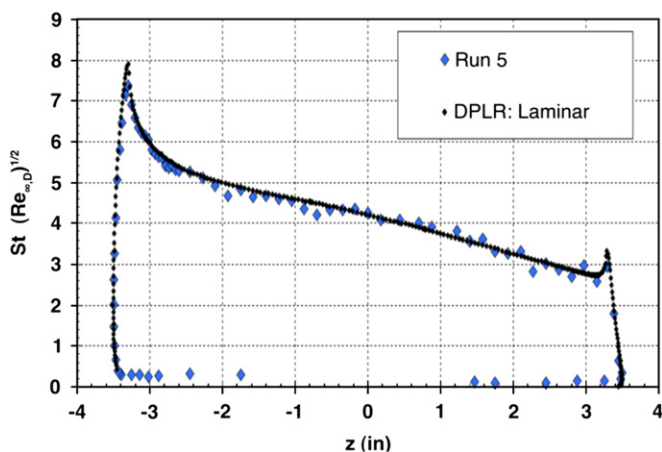


Fig. 7. CEV Mach 8, $\alpha=20$ -deg laminar data and comparisons from CUBRC LENS-I.

Comparisons are shown in Figs. 7 and 8. Good agreement was achieved, although the turbulent data for the windward corner are not shown due to multi-dimensional conduction effects in the wind tunnel model for which corrections have not yet been generated.

2.2.2. AEDC tunnel 9 testing of Orion CEV

Turbulent aeroheating testing of the Orion CEV vehicle was also conducted [22] in the AEDC Hypervelocity Wind Tunnel No. 9 on a 7-in. diameter, thermocouple-instrumented model in perfect-gas N_2 flow at the tunnels Mach 8 and Mach 10 test conditions. Angles-of-attack were varied from 16-deg to 32-deg. Free stream Reynolds numbers ranged from 8×10^6 /ft to 48×10^6 /ft at Mach 8 and from 2×10^6 /ft to 20×10^6 /ft at Mach 10. Transitional or turbulent flow was produced on the heat shield leeside for $Re_{\infty} \geq 10 \times 10^6$ /ft for both Mach 8 and Mach 10, while for the higher Mach 8 Reynolds numbers ($Re_{\infty} \geq 32 \times 10^6$ /ft), turbulent flow was also produced on the wind side of the heat shield. The experimental uncertainty of the data was estimated to be $\pm 12\%$.

Laminar and turbulent perfect-gas comparisons to these data were performed using the LAURA code [30] with the algebraic Cebeci-Smith turbulent model being used for the turbulent cases. Comparisons between centerline data and predictions are shown for selected $\alpha=28$ -deg cases in Figs. 9 and 10. Free stream conditions for these cases are listed in Table 3. For the Mach 10 cases (Fig. 9), the laminar predictions and data were in close agreement at the $Re_{\infty}=4 \times 10^6$ /ft case, while at $Re_{\infty}=19 \times 10^6$ /ft, the laminar predictions matched the data on the windside of the forebody and the turbulent predictions matched the data on the leeside. For both Mach 8 cases (Fig. 10), the turbulent predictions matched the data.

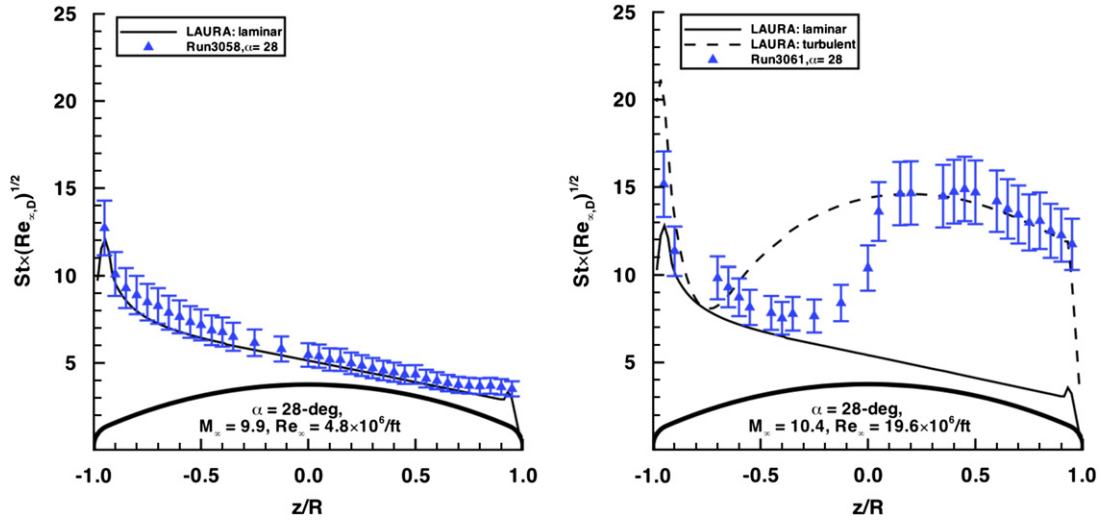
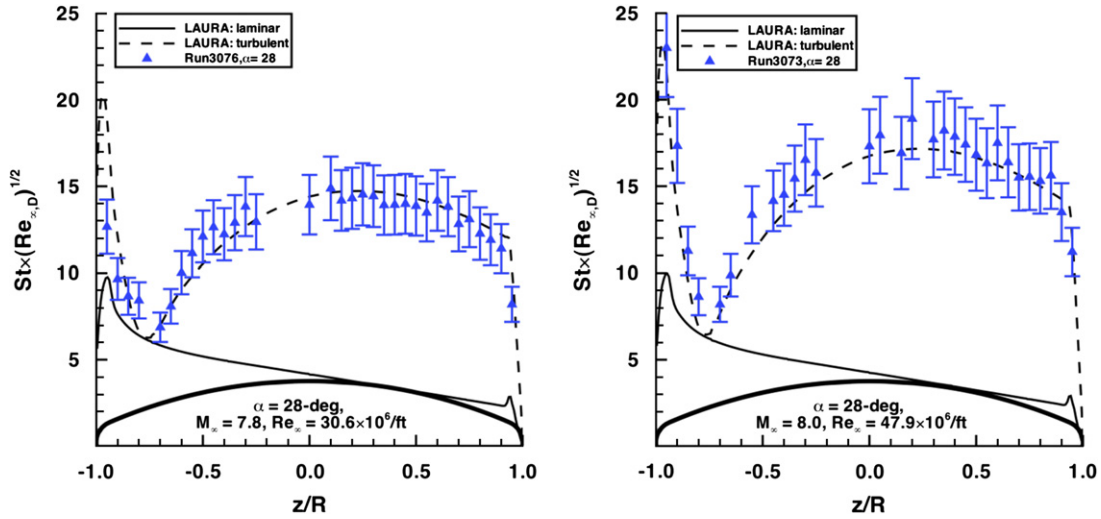
Fig. 9. CEV Mach 10, $\alpha=28$ -deg data and comparisons from AEDC Tunnel 9.Fig. 10. CEV Mach 10, $\alpha=28$ -deg data and comparisons from AEDC Tunnel 9.

Table 3
CEV test conditions for AEDC Tunnel 9.

Run	α (deg.)	Re_{∞} (1/ft)	M_{∞}	P_{∞} (Pa)	T_{∞} (K)	ρ_{∞} (kg/m ³)	U_{∞} (m/s)
3058	28	4.58E+06	9.85	622	54.4	0.0358	1483
3061	28	1.97E+07	10.42	2120	48.4	0.148	1478
3076	28	3.07E+07	7.80	8290	74.1	0.378	1367
3073	28	4.79E+07	7.96	11,800	70.6	0.566	1360

2.2.3. LaRC 20-Inch Mach 6 air testing of Orion CEV

An aeroheating test of the Orion CEV was conducted [21] in the NASA LaRC 20-Inch Mach 6 Air Tunnel [33]. Data were obtained on a 7-in. diameter model using the global phosphor thermography technique [34] with an estimated experimental uncertainty of $\pm 10\%$. Testing was conducted at 28-deg angle of attack with free stream Reynolds numbers from of $2.0 \times 10^6/\text{ft}$ to $7.3 \times 10^6/\text{ft}$. At these conditions, discrete boundary-layer trips located downstream of the stagnation point were required to produce fully-turbulent leeside flow.

Laminar and turbulent perfect-gas comparisons to these data were performed using the LAURA code [30] with the algebraic Cebeci–Smith turbulent model being used for the turbulent cases.

Comparisons between centerline data and predictions are shown for selected $\alpha=28$ -deg cases in Fig. 11. Free stream conditions for these cases are listed in Table 4. Laminar predictions upstream of the trip locations were in good agreement with the data, as were both fully-turbulent and tripped boundary layer computations with the data downstream of the trip location.

3. Non-equilibrium blunt-body flow

At higher enthalpies such as experienced during atmospheric re-entry, chemical and vibrational non-equilibrium effects behind the shock wave become significant, especially for the strong shock waves generated by blunt bodies. In comparison to perfect-gas or equilibrium problems, much more complex computational methods are required to model the various associated chemical reactions, vibrational excitation and relaxation rates, transport processes, and catalytic effects. Validation of these methods is challenging—few ground test facilities are capable of simulating these high enthalpies (let alone maintaining the correct Mach and Reynolds number levels) and collection of data from actual missions or flight tests is both expensive and technically complex.

As noted in the previous section, both the MSL and Orion CEV will experience atmospheric entry at relatively high speeds (CEV

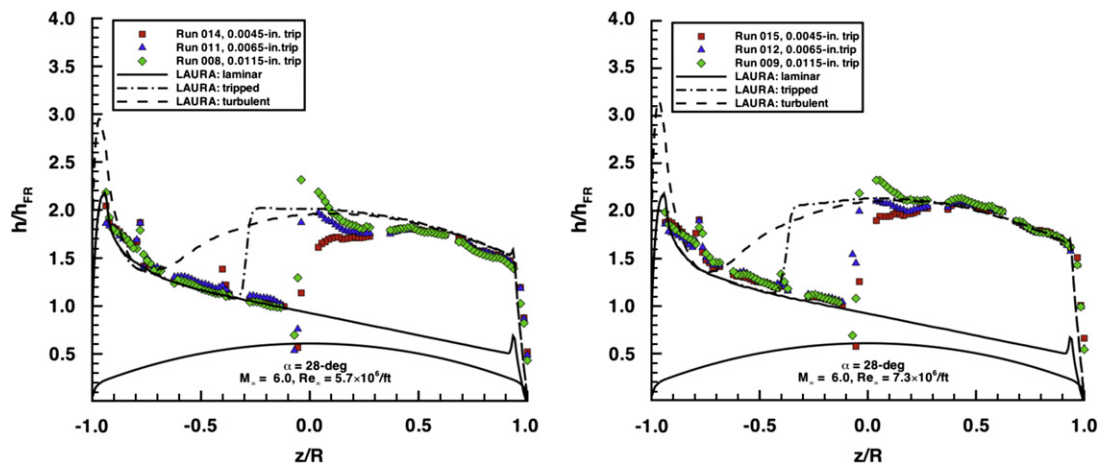


Fig. 11. CEV Mach 6, α =28-deg data and comparisons from LaRC 20-Inch Mach 6 Air Tunnel.

Table 4
CEV test conditions for LaRC 20-Inch Mach 6 Air Tunnel.

Run	α (deg.)	Re_∞ (1/ft)	M_∞	P_∞ (Pa)	T_∞ (K)	ρ_∞ (kg/m ³)	U_∞ (m/s)
3058	28	5.7E+06	6.0	1593	63.1	0.0881	958
3073	28	7.3E+07	6.0	2043	63.1	0.0113	959

Table 5
MSL test conditions for CUBRC LENS-I.

Run	α (deg.)	Re_∞ (1/ft)	M_∞	P_∞ (Pa)	T_∞ (K)	ρ_∞ (kg/m ³)	U_∞ (m/s)	[CO ₂]	[CO]	[O ₂]	[O]
8	0	1.14E+05	6.2	1613	892	0.00896	2871	0.8630	0.0872	0.0497	0.0001

at ~ 11 km/s at Earth and MSL at ~ 5 km/s at Mars), which, in addition to producing transition to turbulence, will also produce thermochemical non-equilibrium effects. Test programs have been conducted for both missions with the goal of obtaining high-enthalpy heating data for code validation purposes.

3.1. Mars Science Laboratory non-equilibrium flow

3.1.1. CUBRC LENS testing of MSL

Testing of the MSL entry vehicle was performed with CO₂ as the test gas in the LENS I reflected shock tunnel [5, 8] to obtain high-enthalpy, turbulent aeroheating data. Two tests were conducted; one with a 24-in. (0.6096 m) diameter model with thin-film gages and coaxial surface thermocouples and one with a 12-in. (0.3048 m) diameter model with coaxial surface thermocouples, thin-film gages, and calorimeter gages. Testing was conducted at enthalpies in the 5 MJ/kg to 10 MJ/kg range at angles-of-attack of 0-deg to 20-deg. Supporting CFD simulations for these tests were performed using both the DPLR [32] and LAURA [30] codes. Discussion herein will focus on a 5 MJ/kg, 0-deg angle-of-attack, 12-in. model case with conditions listed in Table 5.

Owing to the presence of significant levels of free stream vibrational non-equilibrium these tests were not ideal for the stated goal of obtaining high-fidelity data for CFD validation. The presence of free stream vibrational non-equilibrium was noted when a comparison of predicted and measured shock shapes (e.g. Fig. 12) were found to have large differences that were not evident in CO₂ tests in other facilities or in the LENS-X expansion tunnel (Fig. 13). However, these data did highlight several critical issues for CFD simulation of high-enthalpy flows including: the requirement for including free stream non-equilibrium vibrational excitation in a reflected shock tunnel simulation; the uncertainties in the application of Park's two-temperature model

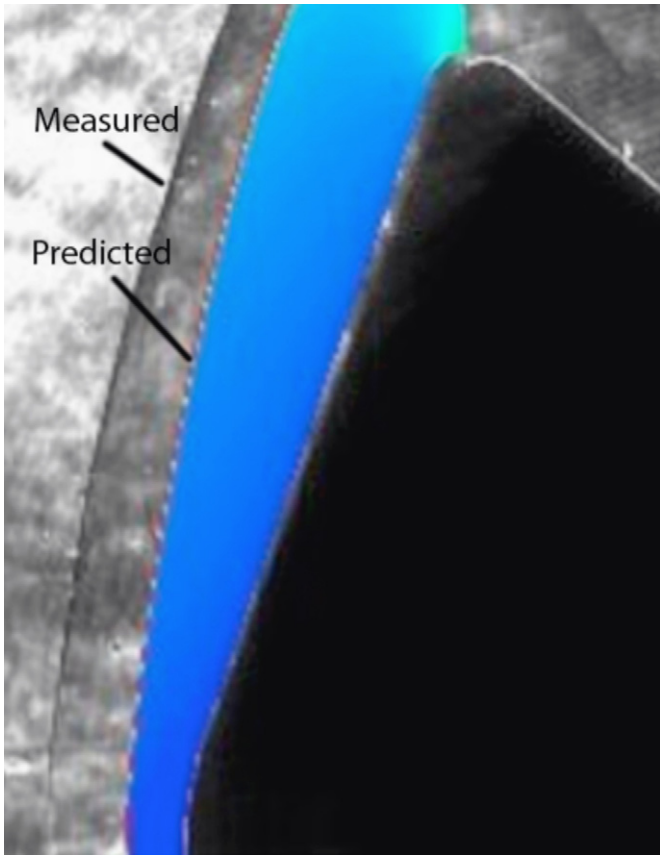


Fig. 12. Comparison between measured and predicted shock shape for MSL in CUBRC LENS-I.

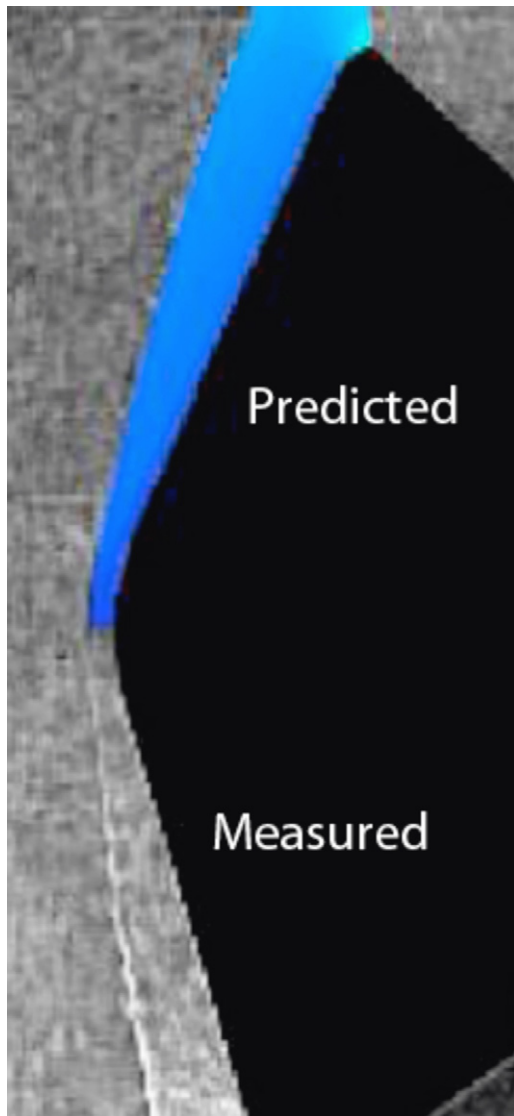


Fig. 13. Comparison between measured and predicted shock shape for MSL in CUBRC LENS-X.

[35] to CO_2 ; the uncertainties in surface catalytic models for CO_2 (both for actual vehicle heat shield materials and for metallic wind tunnel model surfaces); and the interactions between vibrational excitation, transport processes, and surface catalytic effects on heating.

The hypothesized presence of frozen vibrational flow in the free stream led to examination of the validity of Park's two-temperature translational/vibrational temperature model for simulation of CO_2 . Unlike the diatomic N_2 and O_2 molecules for which Park developed this model, that have a single vibrational mode, the triatomic CO_2 molecule has three vibrational modes. Current CFD codes employed in the design of MSL (LAURA and DPLR) use variations of Park's model (with different options available for modeling the vibrational relaxation rates). It was estimated that the resultant sensitivities in the existing two-temperature model options could introduce at least a $\pm 1\%$ uncertainty in the MSL vehicle's trim angle during certain parts of the trajectory, while the actual accuracy of the two-temperature model itself is unknown. Such uncertainties have the potential to significantly affect the landing accuracy of the vehicle.

The wall boundary catalytic efficiency assumption was found to have a large effect on the predicted heat-transfer rates as

shown in Fig. 14. At laminar conditions, the predictions matched the data better when the assumption of a fully-catalytic wall (recombination to free stream species concentrations) was made, whereas predictions with a non-catalytic wall were much lower than the data. However, it is questionable whether the wind tunnel model material could truly behave as a super-catalytic surface.

As noted previously, differences in the predicted and measured shock shapes led to the theory that vibrational non-equilibrium effects were present in the free stream. While the actual free stream state in the facility could not be accurately determined, a parametric computational analysis [8] was performed using the DPLR [32] code in which the assumed energy in the vibrational mode was varied until the predicted shock-shapes could be brought into agreement with the measured data. As shown in Fig. 15 the free stream vibrational non-excitation also had

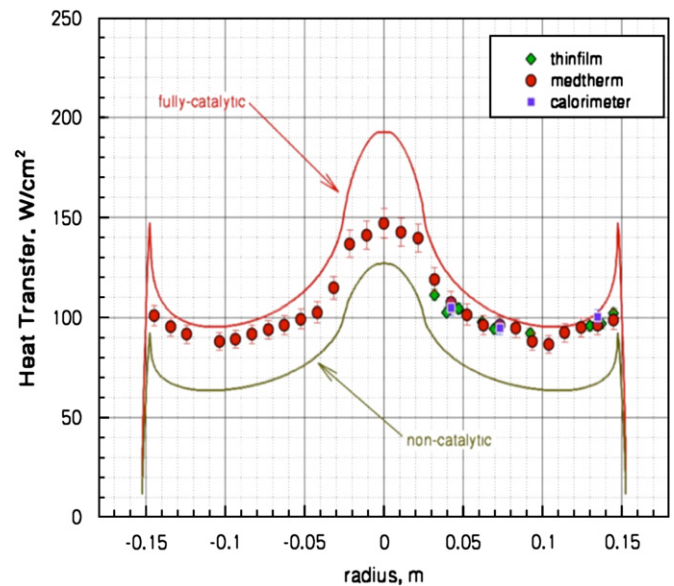


Fig. 14. Comparison between super-catalytic and non-catalytic heating predictions for MSL 12-in. model, CUBRC LENS-1, Run 8.

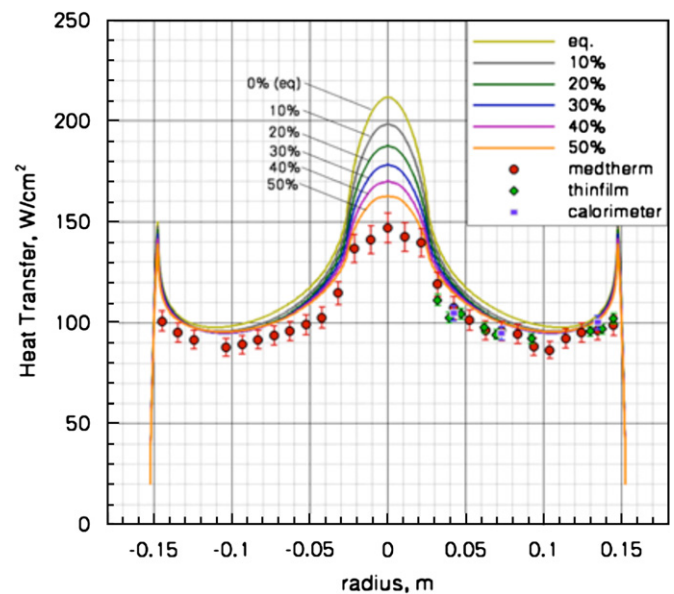


Fig. 15. Effects of free stream vibrational non-equilibrium on heating predictions for MSL 12-in. model, CUBRC LENS-1, Run 8.

Table 6
MSL high-enthalpy test conditions for Caltech T5.

Run	α (deg.)	Re_∞ (1/ft)	T_∞ (K)	ρ_∞ (kg/m ³)	U_∞ (m/s)	H0 (MJ/kg)	[CO ₂]	[CO]	[O ₂]	[O]
2257	11	2.21E+05	2342	0.0549	3550	11.7	0.5379	0.2989	0.1357	0.0274
2258	11	6.68E+05	1351	0.0156	2552	4.9	0.9549	0.0301	0.0151	0.0000

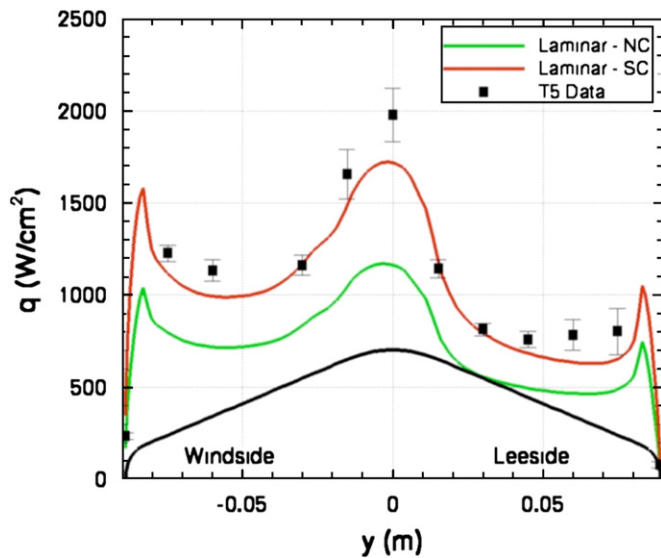


Fig. 16. Comparison between super-catalytic and non-catalytic laminar heating predictions for MSL in CalTech T5 Run 2257.

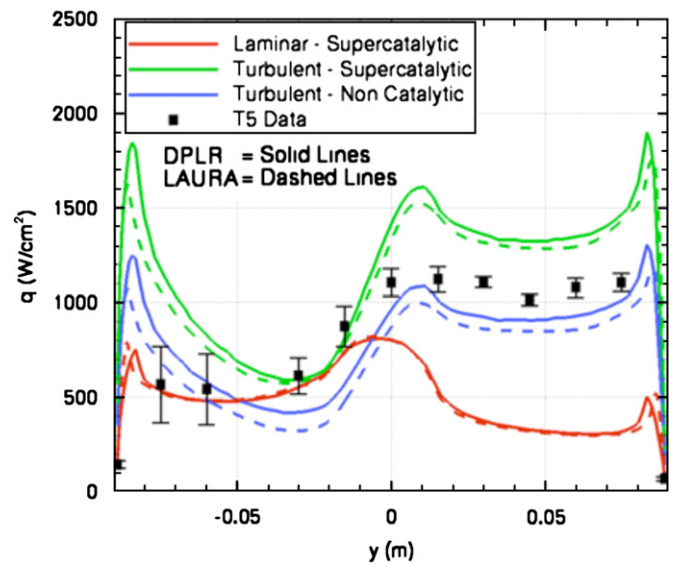


Fig. 17. Comparison between super-catalytic and non-catalytic turbulent heating predictions for MSL in CalTech T5 Run 2258.

a significant effect on the computed stagnation region heating. It was found that an assumed free stream vibrational non-equilibrium level of $\sim 42\%$ was required to reconcile the measured and predicted shock stand-off distance; although these levels are high, they are smaller magnitude than the reservoir non-equilibrium levels. Similar effects were also found for assumed fractions of free stream chemical non-equilibrium.

3.1.2. Caltech T5 testing of MSL

Testing of the MSL entry vehicle was also conducted in CO₂ test gas in the California Institute of Technology (Caltech) T5 reflected shock tunnel [11]. The wind tunnel model had a 7-in. (0.1778 m) diameter and was instrumented with coaxial surface thermocouples. Enthalpy levels varied from 5 MJ/kg to 15 MJ/kg and angles-of-attack varied from 0-deg to 16-deg. Supporting CFD predictions were performed using the DPLR [32] code. Test conditions for sample cases are given in Table 6.

At the test conditions generated in T5, the free-stream vibrational non-equilibrium problem experienced in the CUBRC LENS tests did not appear to be significant since predicted and measured shock shapes were found to be in close agreement. However, the question of surface catalysis was still found to be important. As shown in Fig. 16, at conditions for which the boundary layer was assumed to be fully laminar, the data and predictions were found to be in relatively close agreement with the assumption of a super-catalytic boundary wall boundary conditions—that is, full recombination to free stream species distributions. However, for conditions at which the boundary layer was assumed to be fully turbulent, the data and predictions were found to agree best when the opposite assumption of a non-catalytic wall boundary condition was made, as shown in Fig. 17.

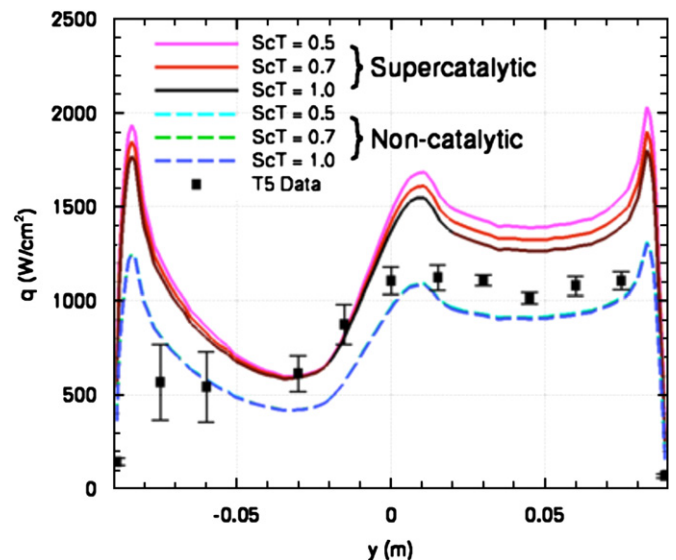


Fig. 18. Effect of turbulent Schmidt number on predictions for MSL in CalTech T5 Run 2258.

The comparison in Fig. 17 is for turbulent predictions using the algebraic Baldwin–Lomax model, with an assumed turbulent Schmidt number of 0.5. A small, but noticeable effect on predicted heating levels for the super-catalytic case – but not the non-catalytic case – was noted when the turbulent Schmidt numbers were varied, as shown in Fig. 18. Additional CFD analyses were performed in which the Baldwin–Lomax model was replaced with

Menter's Shear-Stress Turbulent (SST) model as shown in Fig. 19. While both factors were found to have significant effects on predicted turbulent heating levels, neither effect was large enough to reconcile super-catalytic predictions with the turbulent data.

These results from Caltech T5 and the results from CUBRC LENS in the previous section further highlight the development and validation problems in the modeling of turbulence, catalysis, and chemical and vibrational rates that must be addressed to increase the fidelity on non-equilibrium CO₂ flow field prediction methods. This problem will become greater in importance as future Mars mission requirements call for larger landed masses that lead to greater entry velocities and thus higher heating levels.

3.2. Orion Crew Exploration Vehicle non-equilibrium flow

High-enthalpy testing of an Orion CEV-like geometry was conducted in the CUBRC LENS-I facility in both air and nitrogen [17]. The model size 5.74-in. (0.167 m) in diameter and was instrumented with coaxial surface thermocouples. Data were obtained for angle-of-attack of 0-deg and 28-deg in N₂ at a ~10 MJ/kg total enthalpy and in air at total enthalpies of ~2 MJ/kg to 12 MJ/kg. Sample test conditions for air cases are given in Table 7.

Predictions were performed using the DPLR [32] code with non-catalytic, finite-catalytic, and super-catalytic wall boundary conditions. For the N₂ cases, good agreement with data was observed with small levels of finite catalysis. Results (Figs. 20–23) were less consistent for the air cases; at the lower enthalpy levels, a close agreement was observed with the super-catalytic boundary condition, whereas at the higher enthalpy levels better agreement was observed with the non-catalytic boundary conditions. In these

figures, it can also be seen that the disagreement between measured and predicted surface pressure increased with enthalpy. Additionally, increasing differences between the measured and predicted shock shapes (Fig. 24) were observed with increasing enthalpy; this could indicate either the presence of un-accounted for chemical/vibrational

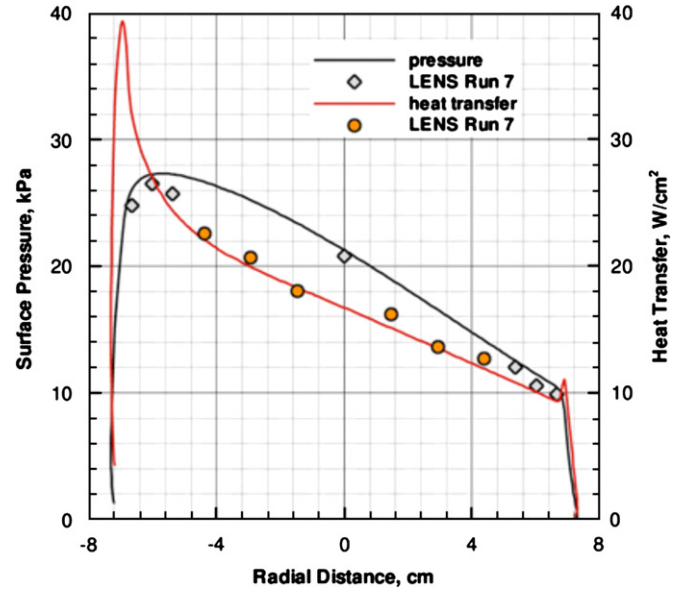


Fig. 20. Comparison between CEV data and predictions for CUBRC LENS-1, Run 7, 1.7 MJ/kg enthalpy.

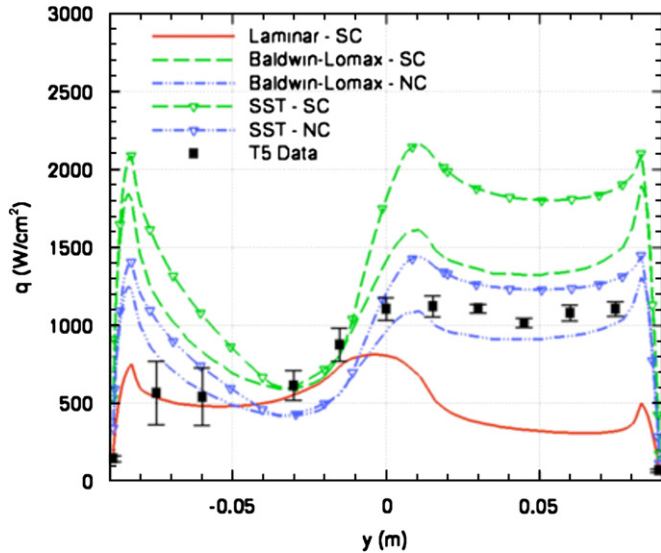


Fig. 19. Comparison between turbulence models predictions for MSL in CalTech T5 Run 2258.

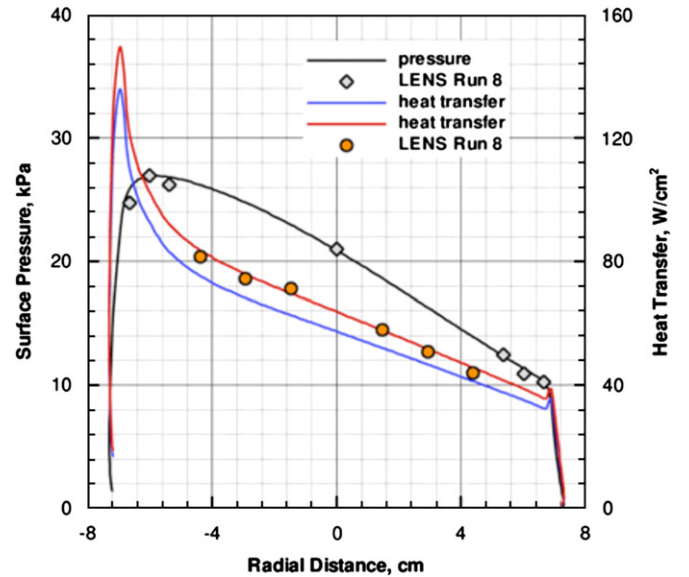


Fig. 21. Comparison between CEV data and predictions for CUBRC LENS-1, Run 8, 4.8 MJ/kg enthalpy.

Table 7
CEV high-enthalpy test conditions for CUBRC LENS-I.

Run	α (deg.)	$T_{\infty}, T_{V\infty}$ (K)	U_{∞} (m/s)	H_0 (MJ/kg)	$\rho_{\infty, N_2} Z$ (kg/m ³)	$\rho_{\infty, O_2} Z$ (kg/m ³)	$\rho_{\infty, NO}$ (kg/m ³)	$\rho_{\infty, O}$ (kg/m ³)
7	28	57	1805	1.7	6.798E-03	2.144E-03	0.000E+00	0.000E+00
8	28	191	2949	4.8	2.431E-03	6.529E-04	2.339E-04	1.902E-06
9	28	494	4054	9.2	1.214E-03	3.035E-04	9.108E-05	3.402E-05
10	28	631	4601	12.4	7.939E-04	1.493E-04	6.347E-05	6.949E-05

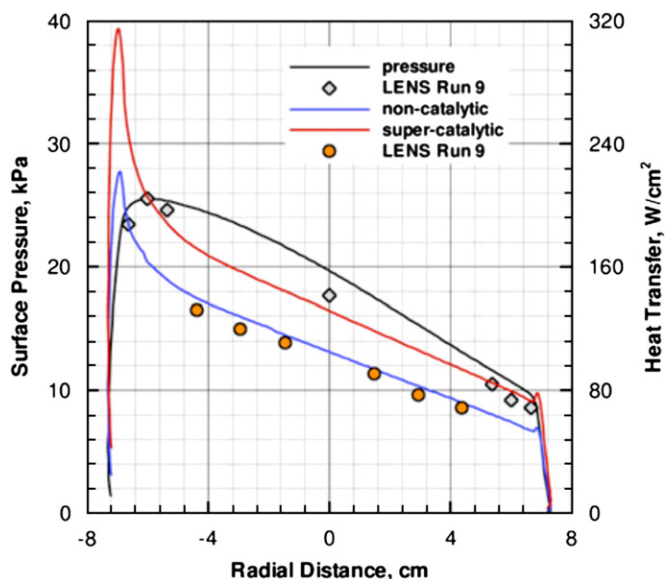


Fig. 22. Comparison between CEV data and predictions for CUBRC LENS-1, Run 9, 9.2 MJ/kg enthalpy.

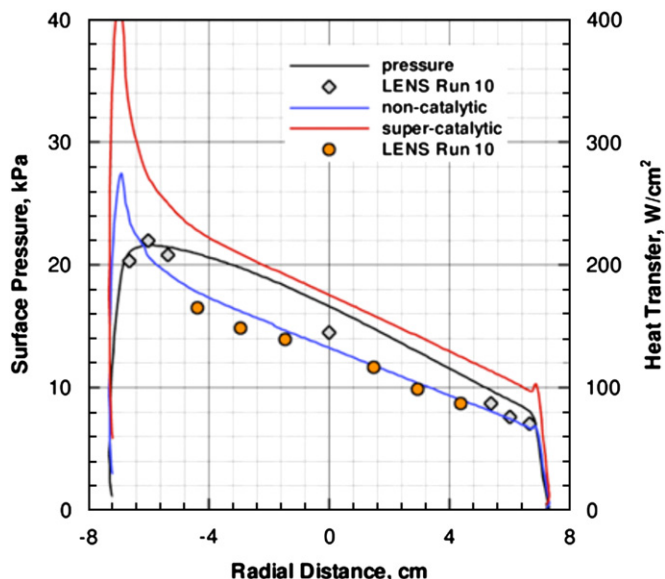


Fig. 23. Comparison between CEV data and predictions for CUBRC LENS-1, Run 10, 12.4 MJ/kg enthalpy.

freezing in the free stream or an inadequacy in the chemical/vibrational computational modeling for air.

4. Rarefied flow

Rarefied flow effects are of importance in high-altitude hypersonic flows where the continuum assumptions inherent to Navier–Stokes based computational tools are inadequate. Comparisons of rarefied flow predictions with experimental data have been previously reported for an MSL-like configuration in [36,37] and little new work has since been performed. As for the CEV, there have as yet been no rarefied flow experiments performed and so aerothermodynamic analyses have been limited to computational studies.

A study [38] has been performed to investigate the overlap between rarefied-flow DSMC computations and continuum-flow Navier–Stokes computations. In this study, the baseline conditions (Table 8) suggested for the CEV are representative of conditions that would take place during the re-entry trajectory from the International Space Station (ISS).

The focus of this work was mainly on the 85 km and 95 km cases; for these two trajectory points, both DSMC and CFD computations were performed in order to evaluate a comparison between molecular approach (i.e., DSMC) and continuum one (i.e., CFD with and without slip flow boundary conditions). As shown in Figs. 25 and 26, surface heating rates computed using DSMC were approximately 10% higher than the CFD results; it is also noticeable that the DSMC results do not indicate the slight rise in heating at the shoulder predicted by the CFD results.

An evaluation of the chemical and conductive contributions to the global heat flux is shown in Fig. 27 for a fully-catalytic boundary condition at 85 km. In particular, it can be seen that the chemical contribution to the heat flux calculated by CFD is very close to that from DSMC, while the conductive contribution is much lower, thus generating a nearly 10% lower total heat flux as predicted by CFD. This difference in global heat flux is shown again for a non-catalytic wall case at 95 km in Fig. 28. It is interesting to note that in the non-catalytic case the percentage difference between CFD and DSMC results increases from about 10% to 60%, but the absolute value of this difference is the same as for fully catalytic wall; this confirms that the discrepancy is not due to the chemical part of the heat flux, but from the conductive one. The same considerations apply to the altitude 95 km case.

The stagnation point heat flux predictions for all cases are summarized in Fig. 29. As a reference, results obtained through the Fay–Riddell formula, typically used for preliminary design of

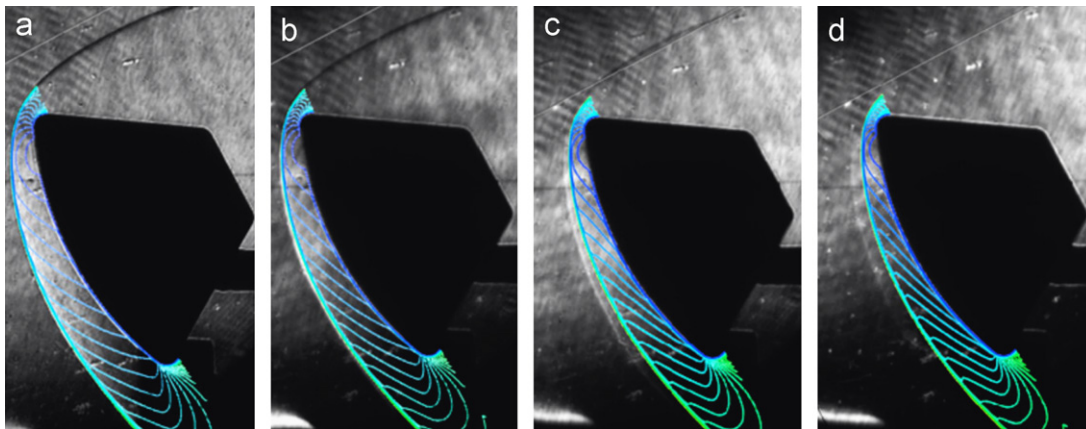


Fig. 24. Comparison between measured and predicted shock shape for CUBRC LENS-1, high-enthalpy CEV test. (a) Run 7, $h_0 = 1.6$ MJ/kg, (b) Run 8, $h_0 = 4.8$ MJ/kg, (c) Run 9, $h_0 = 9.2$ MJ/kg and (d) Run 7, $h_0 = 12.4$ MJ/kg.

Table 8

Representative ISS mission free-stream conditions.

Altitude (km)	α (deg.)	T_∞ (K)	U_∞ (m/s)	ρ_∞ (kg/m ³)	n_∞ (#/m ³)	X_{∞, O_2}	X_{∞, N_2}	$X_{\infty, N}$	T_w (K)	Kn_∞	Computational method
75	0	200	7600	4.34E–05	9.01E+20	0.2372	0.7628	0.0000	1464	0.0003	CFD
85	0	181	7600	7.96E–06	1.65E+20	0.2372	0.7628	0.0000	1184	0.0019	CFD & DSMC
95	0	189	7600	1.38E–06	2.90E+19	0.1972	0.7869	0.0159	951	0.01	CFD & DSMC
105	0	211	7600	2.30E–07	4.98E+18	0.1528	0.7819	0.0653	760	0.06	DSMC
115	0	304	7600	4.36E–08	9.86E+17	0.0979	0.7539	0.1484	618	0.32	DSMC
125	0	433	7600	1.31E–08	3.06E+17	0.0768	0.7117	0.2115	494	1.0	DSMC

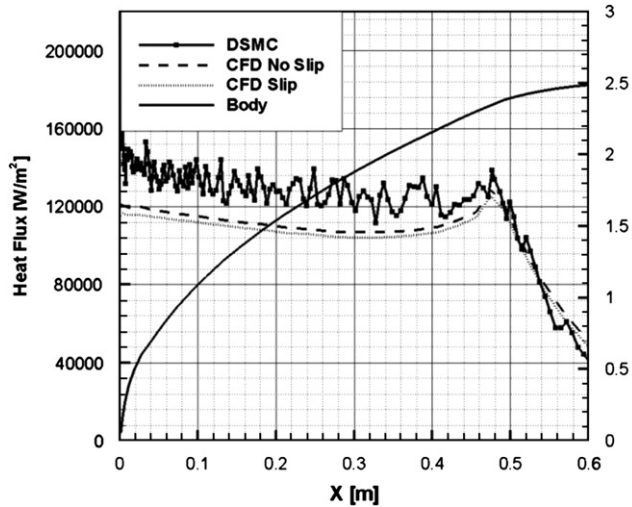


Fig. 25. Predicted CEV heat flux at 85 km.

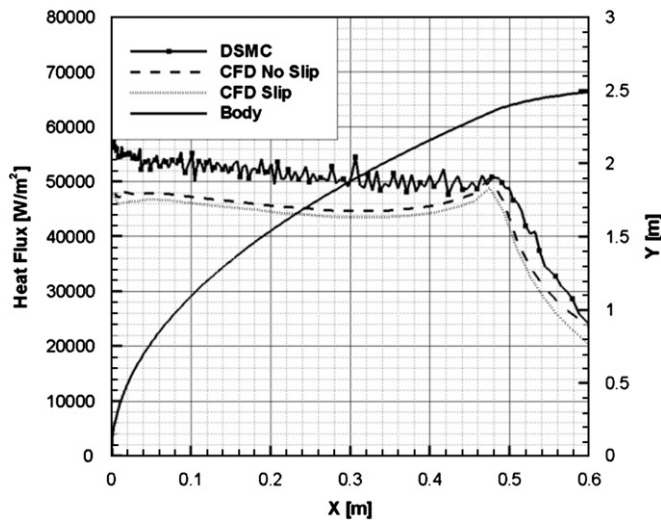


Fig. 26. Predicted CEV heat flux at 95 km.

the Thermal Protection Systems, have been also reported. In the overlap (between 85 km and 95 km), where both modeling methods could be applied, DSMC results are to be preferred for the more correct modeling of rarefaction effects and for more conservative design margins.

5. Radiation transport

Radiation transport becomes an increasingly large contributor to the re-entry vehicle heating environment as either the entry velocity or body diameter increase. In the case of blunt re-entry vehicle such as Apollo or the Orion CEV, radiative heat-transfer

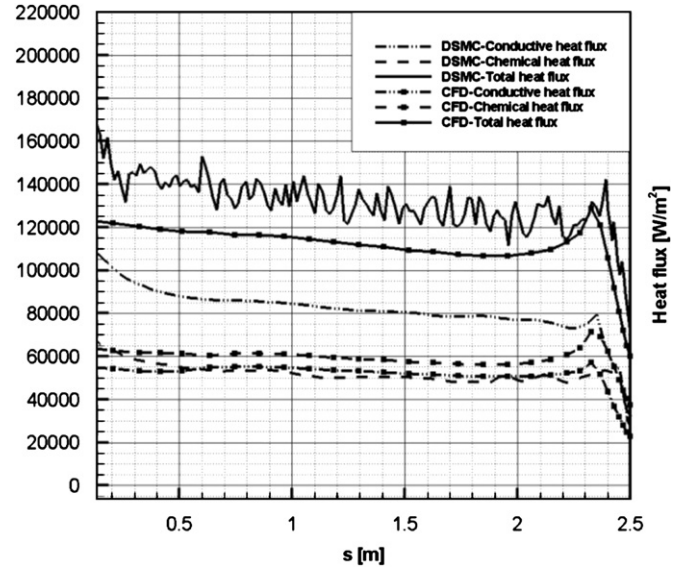


Fig. 27. Chemical and conductive contributions to CEV heat flux at 85 km with fully catalytic wall.

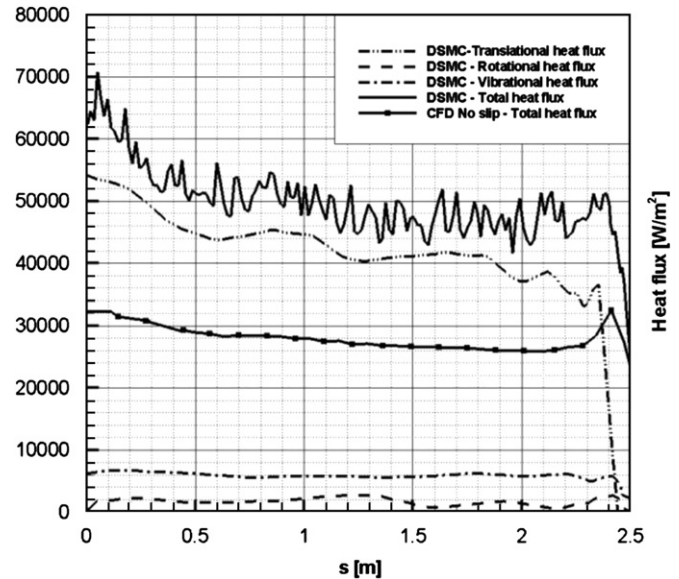


Fig. 28. Chemical and conductive contributions to CEV heat flux at 95 km with non-catalytic wall.

can be of equal to, or greater, magnitude than the convective heating at points along the trajectory. Ground testing capabilities for radiative heating effects on entry vehicles are extremely limited; most ground testing in this field consists of optical diagnostics of shock-tube flows (e.g. [39]) rather than the testing of actual wind tunnel models with radiative heating

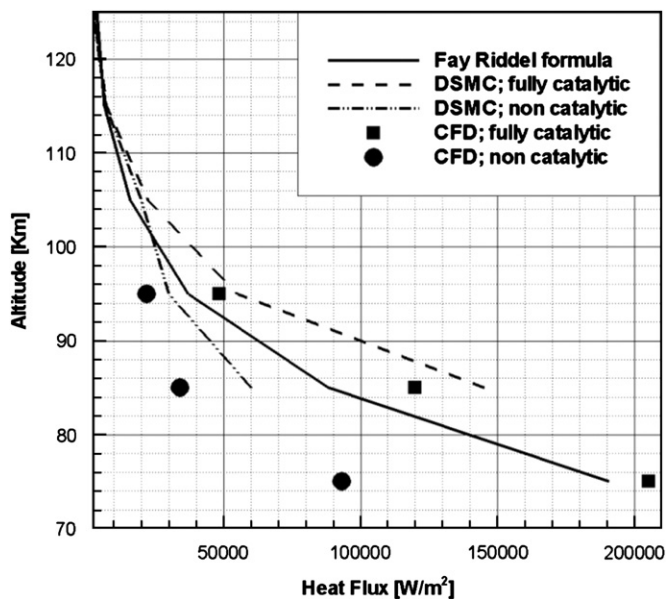


Fig. 29. Stagnation point heat-flux predictions vs. altitude.

Table 9
FIRE-II flight test points.

Time (s)	Alt. (km)	ρ_∞ (kg/m ³)	U_∞ (km/s)	T_∞ (K)	T_{WALL} (K)	Heat-shield
1634.0	76.42	3.72E-5	11.36	195	6.15	First
1636.0	71.02	8.57E-5	11.31	210	810	First
1637.5	67.05	1.47E-4	11.25	228	1030	First
1640.5	59.62	3.86E-4	10.97	254	1560	First
1643.0	53.04	7.80E-4	10.48	276	640	Second
1645.0	48.37	1.32E-3	9.83	285	1520	Third
1648.3	41.60	3.25E-3	8.1	267	503	Third

measurements (e.g. [40]). The acquisition of flight test data is also challenging both due to the cost and complexity of instrumentation and measurements as well as the difficulty of separating radiative heating effects from those of convective heating and ablation cooling of real TPS systems.

5.1. FIRE-II radiation transport

Numerous studies have been published with comparisons to the FIRE II data; however, most of these studies applied older computational tools and methods that are no longer in use. One of the most recent studies [41] was conducted using the HARA radiation transport code [42,43]. The HARA code includes detailed line radiation models based on the latest National Institute of Standards and Technology (NIST) atomic data, a smeared rotational band model for molecular radiation, and non-Boltzmann populations of excited states. In this study, the radiation transport code and a viscous shock-layer code were run in a loosely-coupled mode in order to account for the flow field energy loss due to radiation.

Computations were performed for each of the three heat-shields at the times given in Table 9. Radiation-flow field coupling was found to reduce the radiative heating by up to 30% as shown in Figs. 30 and 31. It was also found that the radiation from the vacuum-ultraviolet region, which was neglected in some prior studies, was a significant contributor to the total flux. Comparisons were made between predicted and inferred radiative stagnation-point heat flux in the (0 eV–6 eV) and in the (6 eV–18 eV) ranges as shown in Table 10. The ‘inferred’ radiative heat flux for

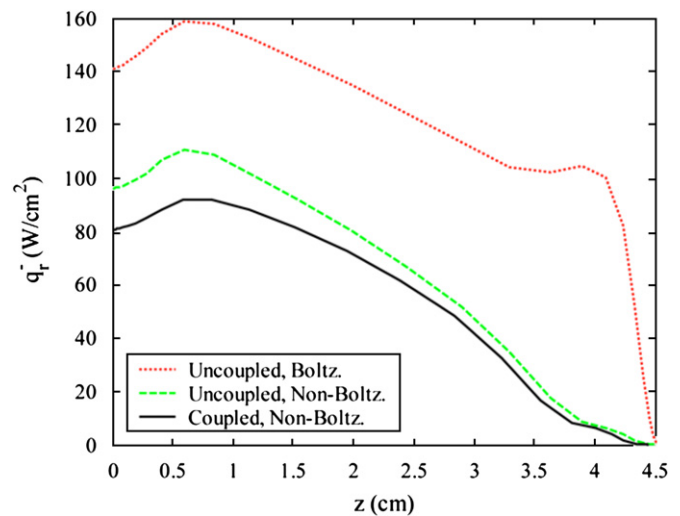


Fig. 30. FIRE-II, $t=1636$ s: Stagnation line radiative flux computations showing effects of flow field/radiation coupling.

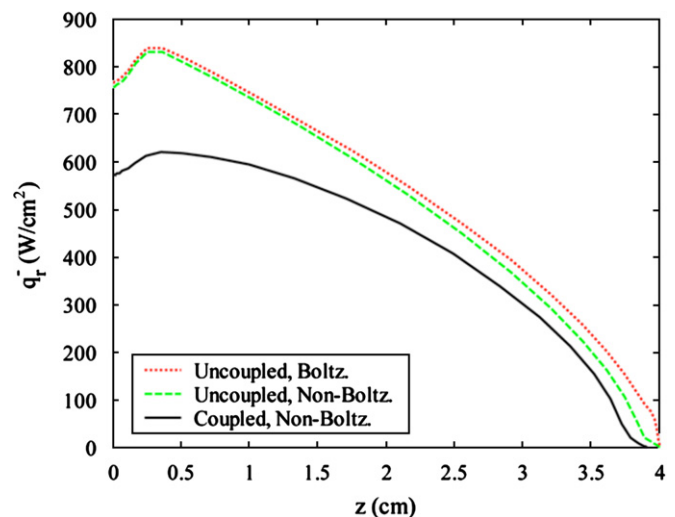


Fig. 31. FIRE-II, $t=1643$ s: Stagnation line radiative flux computations showing effects of flow field/radiation coupling.

the (6 eV–18 eV) range is taken to be the measured *total* heating at the calorimeter (radiative+convective) minus the integrated spectrometer measurement for the (0 eV–6 eV) range, minus the *predicted* convective heat flux computed using either non-catalytic or super-catalytic surface boundary conditions assumption. This inference was necessary because there were no direct measurements of total radiative heat-flux; rather, measurements were made of total heat flux and both spectral and integrated radiative intensities (over different frequency intervals). The actual heat-shield surface catalytic effectiveness would have been somewhere between these two extremes; note that at the theoretical upper bound of super-catalytic effectiveness, it would actually be necessary for the radiative heating to be negative since the predicted super-catalytic convective result exceeds the total calorimeter measurement.

6. Summary, conclusions, and recommendations

Several examples have been presented in which modern computational tools and methods have been compared to either ground test or flight test data on blunt body reentry vehicles.

Table 10

Comparison of predicted and inferred absorbed radiative flux for FIRE-II.

Time (s)	(0 eV–6 eV) range			(6 eV–18 eV) range				
	Measured flux (W/cm ²)	Predicted flux (W/cm ²)	% difference	Inferred super-catalytic flux (W/cm ²)	Inferred non-catalytic flux (W/cm ²)	Predicted flux (W/cm ²)	Super-catalytic % difference	Non-catalytic % difference
1634.0	3.4	4.5	32	–45.4	58.6	10.1	NA	–83
1636.0	12.9	14.2	10	26.9	90	36.3	35	–60
1637.5	31.4	29.8	–5	–1.6	126	71.3	NA	–43
1640.5	81.7	95.2	17	133	258	166.6	25	–35
1643.0	151	135.2	–10	141	220	179.4	27	–18
1645.0	63.9	91	42	259	345	85.8	–67	–75
1648.3	8.1	267	503	–16	64	10.5	NA	–84

These comparisons have highlighted the effectiveness of the computations at predicting the effects of physical phenomena such as turbulence, chemical and vibrational non-equilibrium, rarefied flow, and radiation transport.

Of these phenomena, the best comparisons have been obtained for turbulent data. However these studies were all performed at perfect-gas conditions, and thus there still exists the need to validate computational models at non-equilibrium conditions for both Earth and Mars atmospheric environments.

With respect to non-equilibrium, greater discrepancies have been found between data and predictions. The accuracy of chemical and vibrational models has not been fully-validated, especially for Martian CO₂ environments. Additionally, there are difficulties in the analysis of the experimental data itself, both due to the issue of free stream non-equilibrium effects in the test facilities and due to the difficulty in determining the actual catalytic efficiency of the test model.

The validation of radiative transport models is the least advanced, owing both to the complexity of the physical phenomena and to the difficulty of performing ground test simulations or obtaining flight test data. Furthermore, computational predictions are challenging as both flow-field and radiation-transport methods must be coupled in order to properly model the physics of the problem.

Detailed information on each of the test cases presented herein is available and it is recommended that each be studied further in detail and used in the assessment of modern computational tools. However, these data sets themselves have significant uncertainties and are not inclusive enough of all physical situations to be considered adequate to fully-validate numerical tools used in the design of an actual reentry vehicle. At best, these data can help to provide conservative upper bounds on the uncertainties of predictive methods. It is therefore recommended that both ground testing and flight testing of blunt body aerothermodynamic phenomena, coupled to computational predictions and analysis, be rigorously pursued, and that aerothermodynamic instrumentation be included as an integral part of all future missions.

Acknowledgments

The authors wish to acknowledge the contributions to this work provided by: Karen Berger and Christopher Johnston at the NASA Langley Research Center, Michael Wright at the NASA Ames Research Center, and Matt MacLean at CUBRC.

References

- [1] Davies C. "Planetary Mission Entry Vehicles Quick Reference Guide, Version 3.0". NASA SP2006-3401; 2006.
- [2] Prakash R. et al. Mars science laboratory entry, descent, and landing system overview. IEEE Paper 2008-1531. In: Proceedings of the IEEE aerospace conference, Big Sky, MT; March 1–8, 2008.
- [3] Edquist KT, Dyakonov AA, Wright MJ, Tang CY. Aerothermodynamic design of the Mars science laboratory heatshield, AIAA Paper 2009-4075. In: Proceedings of the 41st AIAA thermophysics conference, San Antonio, TX; June 22–25, 2009.
- [4] Wright MJ, Beck RAS, Edquist KT, et al. Sizing and margins assessment of the Mars science laboratory aeroshell thermal protection system, AIAA Paper 2009-4231. In: Proceedings of the 41st AIAA thermophysics conference, San Antonio, TX; June 22–25, 2009.
- [5] Hollis BR, Liechty DS, Wright MJ, Holden MS, Wadhams TP, MacLean M. Transition onset and turbulent heating measurements for the Mars science laboratory entry vehicle, AIAA Paper 2005-1437. In: Proceedings of the 43rd AIAA aerospace sciences meeting and exhibit, Reno, NV; January 10–13, 2005.
- [6] MacLean M, Wadhams T, Holden M, Hollis BR. Investigation of blunt bodies with CO₂ test gas including catalytic effects, AIAA Paper 2005-4693. In: proceedings of the 38th AIAA thermophysics conference, Toronto, Ontario; June 6–9, 2005.
- [7] MacLean M, Holden M. Catalytic effects on heat transfer measurements for aerothermal studies with CO₂, AIAA Paper 2006-0182. In: proceedings of the 44th AIAA aerospace sciences meeting and exhibit, Reno, NV; January 9–12, 2006.
- [8] MacLean M, Holden M. Numerical assessment of data in catalytic and transitional flow for martian Entry. In: Proceedings of the 9th AIAA/ASME joint thermophysics and heat transfer conference, San Francisco, CA; June 5–8, 2006.
- [9] Liechty DS, Hollis BR. Mars science laboratory experimental aerothermodynamics with effects of cavities and control surfaces. Journal of Spacecraft and Rockets 2006;43(2):340–53.
- [10] Hollis BR, Liechty DS. Transition due to heat-shield cavities on a Mars entry vehicle. Journal of Spacecraft and Rockets 2006;43(2):354–66.
- [11] Wright MJ, Olejniczak J, Brown JL, Hornung HG, Edquist KT. Modeling of shock tunnel aeroheating data on the Mars science laboratory aeroshell. Journal of Thermophysics and Heat Transfer 2006;20(4):641–51.
- [12] Hollis BR, Collier BR. Turbulent aeroheating testing of Mars science laboratory entry vehicle. Journal of Spacecraft and Rockets 2008;45(3):417–27.
- [13] Anon. "NASA's exploration systems architecture study, Final Report". NASA TM-2005-214062; November 2005.
- [14] Grinstead JH, Wilder MC, Olejniczak J, Bogdanoff DW, Allen GA, Dang K, et al. Shock-heated air radiation measurements at lunar return conditions, AIAA Paper 2008-1244. In: Proceedings of the 46th AIAA aerospace sciences meeting and exhibit, Reno, NV; January 7–10, 2008.
- [15] Amar AJ, Horvath TJ, Hollis BR, Berger KT, Berry SA, Calvert N. Protuberance boundary layer transition for Project Orion crew Entry Vehicle, AIAA Paper 2008-1227. In: Proceedings of the 46th AIAA aerospace sciences meeting and exhibit, Reno, NV; January 7–10, 2008.
- [16] Liechty DS. Aerothermodynamic testing of protuberances and penetrations on the NASA Crew Exploration Vehicle heat shield, AIAA Paper 2008-1240. In: Proceedings of the 46th AIAA aerospace sciences meeting and exhibit, Reno, NV; January 7–10, 2008.
- [17] MacLean M, Mundy E, Wadhams T, Holden M, Parker R. Analysis and ground test of aerothermal effects on spherical capsule geometries, AIAA Paper 2008-4273. In: Proceedings of the 38th fluid dynamics conference and exhibit, Seattle, WA; June 23–26, 2008.
- [18] Hollis BR. Heating augmentation in laminar flow due to heat-shield cavities on the Project Orion CEV, AIAA Paper 2008-6558. In: Proceedings of the AIAA atmospheric flight mechanics conference and exhibit, Honolulu, HI; August 18–21, 2008.
- [19] Wadhams TP, Cassidy AM, MacLean M, Holden MS. Experimental studies of the aerothermal characteristics of the Project Orion CEV Heat Shield in high speed transitional and turbulent flows, AIAA Paper 2009-0677. In: Proceedings of the 47th AIAA aerospace sciences meeting, Orlando, FL; January 5–8, 2009.
- [20] Hollis BR. Heating augmentation due to compression pad cavities on the Project Orion CEV Heat Shield, AIAA Paper 2009-3843. In: Proceedings of the 41st AIAA thermophysics conference, San Antonio, TX; June 22–25, 2009.
- [21] Berger KT. Aerothermodynamic testing of the crew exploration vehicle at Mach 6 and Mach 10. Journal of Spacecraft and Rockets 2009;46(4):758–65.
- [22] Hollis BR, Berger KT, Horvath TJ, Coblish JJ, Norris JD, Lillard RP, et al. Aeroheating testing and predictions for project Orion Crew Exploration Vehicle. Journal of Spacecraft and Rockets 2009;46(4):766–80.

- [23] Berry SA, Horvath TJ, Lillard RP, Kirk BS, Cassady AM. Aerothermal testing for project Orion Crew Exploration Vehicle, AIAA Paper 2009-3842. In: Proceedings of the 41st AIAA thermophysics conference, San Antonio, TX; June 22–25, 2009.
- [24] Lewis JH, Jr. Scallion WI. Flight parameters and vehicle performance for Project Fire Flight II, Launched May 22, 1965, NASA TN-D-3569; August, 1966.
- [25] Richardson NR. Project fire instrumentation for radiative heating and related measurements NASA TN-D-36461966.
- [26] Cornette ES. Forebody temperatures and calorimeter heating rates measured during Project Fire II reentry at 11.35 km NASA TM-X-13051966.
- [27] Cauchon DL, McKee CW, Cornette ES. "Spectral measurements of gas-cap radiation during project fire flight experiments at reentry velocities near 11.4 km". NASA TM-X-13891967.
- [28] Cauchon DL. "Radiative Heating Results from the Fire II Flight Experiment at a Reentry Velocity of 11.4 km". NASA TM-X-14021967.
- [29] Marren D, Lafferty J. The AEDC Hypervelocity Wind Tunnel 9. Advanced hypersonic test facilities, progress in aeronautics and astronautics, vol. 198. Reston, VA: American Institute of Aeronautics and Astronautics; 2002. [p. 467–477].
- [30] Cheatwood FM, Gnoffo PA. "User's manual for the Langley aerothermodynamic upwind relaxation algorithm (LAURA)". NASA TM 46741996.
- [31] Holden MS, Wadhams TP, Candler GV. Experimental studies in the LENS shock tunnel and expansion tunnel to examine real-gas effects in hypervelocity flows. AIAA Paper 2004-0916; January 2004.
- [32] Wright MJ, Candler GV, Bose D. Data-parallel line relaxation methods of the Navier Stokes equations. AIAA Journal 1998;36(9):1603–9.
- [33] Micol JR. Langley aerothermodynamic facilities complex: enhancements and testing capabilities. AIAA Paper 98-0147, January 1998.
- [34] Merski NR. Global aeroheating wind-tunnel measurements using improved two-color phosphor thermography methods. Journal of Spacecraft and Rockets 1999;36(2):160–70.
- [35] Park C. Assessment of two-temperature kinetic model for ionizing air. Journal of Thermophysics and Heat Transfer July, 1989;3(3):233–44.
- [36] Saric WS, Muylaert J, Dujarric C. Hypersonic experimental and computational capability, improvement and validation, AGARD AR-319, vol. I; May 1966.
- [37] Muylaert J, Kumar A, Dujarric C. Hypersonic experimental and computational capability, improvement and validation, AGARD AR-319, vol. II; December 1998.
- [38] Votta R, Schettino A, Ranuzzi G, Borrelli S. Hypersonic low density aerothermodynamics of Orion-like exploration vehicle. The Journal of Spacecraft and Rockets 2009;46(4):781–7. [AIAA-42663-356].
- [39] Grinstead JH, Wilder MC, Olejniczak J, Bogdanoff DW, Allen GA, Dang K, et al. Shock-heated air radiation measurements at lunar return conditions, AIAA Paper 2008-1244. In: Proceedings of the 46th AIAA aerospace sciences meeting and exhibit, Reno, NV, January 7–10, 2008.
- [40] Capra BR, Leyland P, Morgan RG. Subscale testing of the FIRE II vehicle in a superorbital expansion tube, AIAA Paper 2004-1298. In: Proceedings of the 42nd AIAA aerospace sciences meeting and exhibit, Reno, NV, January 5–8, 2004.
- [41] Johnston CJ, Hollis BR, Sutton K. Nonequilibrium stagnation-line radiative heating for Fire II, AIAA Paper 2007-3908.
- [42] Johnston CO, Hollis BR, Sutton K. Spectrum modeling for air shock layers at lunar return conditions. Journal of Spacecraft and Rockets 2008;45(5):865–78.
- [43] Johnston CO, Hollis BR, Sutton K. Non-Boltzmann modeling for air shock layers at lunar return conditions. Journal of Spacecraft and Rockets 2008;45(5):879–90.